High-Power CMOS Current Driver With Accurate Transconductance for Electrical Impedance Tomography

Loucas Constantinou, *Student Member, IEEE*, Iasonas F. Triantis, *Member, IEEE*, Richard Bayford, *Member, IEEE*, and Andreas Demosthenous, *Senior Member, IEEE*

Abstract—Current drivers are fundamental circuits in bioimpedance measurements including electrical impedance tomography (EIT). In the case of EIT, the current driver is required to have a large output impedance to guarantee high current accuracy over a wide range of load impedance values. This paper presents an integrated current driver which meets these requirements and is capable of delivering large sinusoidal currents to the load. The current driver employs a differential architecture and negative feedback, the latter allowing the output current to be accurately set by the ratio of the input voltage to a resistor value. The circuit was fabricated in a 0.6-μm high-voltage CMOS process technology and its core occupies a silicon area of 0.64 mm^2. It operates from a ± 9 V power supply and can deliver output currents up to 5 mA p-p. The accuracy of the maximum output current is within 0.41% up to 500 kHz, reducing to 0.47% at 1 MHz with a total harmonic distortion of 0.69%. The output impedance is 665 kΩ at 100 kHz and 372 kΩ at 500 kHz.

Index Terms—Accurate transconductance, bioimpedance, CMOS circuits, current driver, electrical impedance tomography (EIT), high power design.

I. INTRODUCTION

ELECTRICAL IMPEDANCE TOMOGRAPHY (EIT) offers particular promise in the assessment of neonatal lung function because it is as a non-invasive imaging method requiring no collaboration from the infant [1]–[4]. Sinusoidal currents (or voltages [5]) are applied to the surface of the body tissue via electrode pairs and the resulting surface potentials are recorded at several locations of the electrode array in order to obtain a set of bioimpedance measurements [6]. Specialized reconstruction algorithms are then employed to produce a tomographic image [7]. The high air content of the lung can provide high contrast images as the impedance of the air is much higher than that of the surrounding tissue. Absolute lung resistivity can be associated with structural characteristics and tissue composition which can be useful in the identification of certain health conditions in neonatal lungs [4].

Current drivers are key devices in EIT systems. For accurate current delivery to the tissue load a current driver should have high output impedance over the total bandwidth of operation. In the case of neonatal lung function monitoring the frequency range is typically 4 kHz to 813 kHz [4] and an output current accuracy of better than 0.5% is desirable. In practice the impedance of the load (electrode-tissue interface) can vary greatly in magnitude. A study of the electrode-tissue impedance characteristic was presented in [8], in which six different types of Ag/AgCl electrodes were evaluated over the frequency range between 10 Hz and 1 MHz. For frequencies below 1 kHz the electrode-tissue impedance was higher than 10 kΩ, reaching values up to 300 kΩ at 10 Hz, and reduced to approximately 1.7 kΩ at 10 kHz, 800 Ω at 50 kHz, 559 Ω at 100 kHz, and 494 Ω at 1 MHz. In another study [9], electrode-tissue impedance characteristics were reported to be around 220 Ω at 100 kHz reducing to 120 Ω at 1 MHz. Exact estimation of the load impedance is a difficult task, thus when dealing with the design of bioimpedance instrumentation a range of load values need to be considered.

The majority of current drivers reported in the literature for EIT and bioimpedance applications are based on discrete electronic designs mostly employing the modified Howland topology [10]. A balanced Howland topology uses a pair of opamps and resistive networks in positive and negative feedback paths. The performance of the Howland topology depends on the specification of the opamps used and the degree of matching of the resistors. The design in [11] used resistors of 0.01% tolerance in order to achieve a high output impedance (1.7 MΩ at 50 kHz). The Howland topology in [12] achieved a measured output impedance of about 750 kΩ at 10 kHz, reducing to 330 kΩ at 300 kHz, and eventually to 70 kΩ at 1 MHz. The maximum output current was limited to 1 mA p-p with an accuracy of about 2% over the total bandwidth. The need for extremely high resistor precision makes the Howland topology unsuitable for integrated circuit design.

L. Constantinou and A. Demosthenous are with the Department of Electronic and Electrical Engineering, University College London, London WC1E 7JE, U.K. (e-mail: loucas.constantinou.10@ucl.ac.uk; a.demosthenous@ucl.ac.uk).

I. F. Triantis was with University College London, London WC1E 7JE, U.K.. He is now with the Department of Electrical and Electronic Engineering, City University, London EC1V 0HB, U.K. (e-mail: iasonas.triantis.1@city.ac.uk).

R. Bayford is with the Department of Health and Social Sciences, Middlesex University, The Burroughs, London NW4 4BT, U.K. (e-mail: r.bayford@mdx.ac.uk).

Other discrete component current driver designs include a topology based on supply current sensing [13] with a measured output impedance of 2.6 MΩ at 100 kHz, reducing to 160 kΩ at 500 kHz. The current driver in [14] used an opamp in inverting configuration with the load present in the negative feedback path. Particular attention was again given to the output impedance characteristic of the circuit and its dependency upon the circuit's components. It achieved a measured output impedance of about 350 kΩ at 50 kHz, reducing to 120 kΩ at 1 MHz. The EIT system in [15] used a current conveyor based current driver, with a measured output impedance of 1.5 MΩ at 10 kHz, reducing to less than 30 kΩ at 500 kHz. A dc suppression feedback loop was utilized to keep the dc output voltage levels to zero. The instrumentation amplifier (IA) based current driver in [16] used digitally-controlled negative capacitance circuits to regulate the circuit's output capacitance and resistance and thus trim the overall output impedance at a specific operating frequency. After trimming the measured output impedance was above 64 MΩ at 30 kHz but temperature variations caused it to drift to a lower value of about 25 MΩ.

A handful of custom integrated current drivers were presented [17]–[21]. The design in [17] used a modification of the supply current sensing scheme [13] with bipolar technology. Simulated results indicated that the circuit's output impedance is 2.5 MΩ at 1 MHz but no measurements were reported. A current driver in 0.18-μm CMOS technology was described in [18] using four current sources implemented in an H-bridge configuration. The circuit used common-mode feedback (CMFB) to control the dc voltage levels at the output nodes. It achieved high output impedance in simulation (10.2 MΩ at 1 MHz) but no measurements were reported. The current driver in [19] also used a standard 0.18-μm CMOS technology. It was designed to operate at 90 kHz and used two fully differential amplifiers to generate the input sinusoidal voltage signal, cascaded by a voltage controlled current source implemented by two transistors and a resistor. Its maximum output current was limited to 350 μA p-p with an accuracy of 1% at 90 kHz. The integrated current driver presented in [21] used an open loop operational transconductance amplifier (OTA) with an active inductive load. It achieved an output impedance in excess of 500 kΩ at 500 kHz but its maximum output current was limited to 500 μA p-p.

We are working on the development of a parallel current drive EIT system with "active" electrodes, primarily for neonatal lung function imaging [1], [7]. The encapsulation of the current driver (and impedance measurement circuitry) within the electrode shell removes lead capacitance problems and therefore enables fast, accurate impedance measurements at relatively high frequencies [22], [23]. A wearable active vest which contains a collection of active electrodes is being developed [24]. Our application requires current drivers with accurate transconductance and capable of generating currents up to 5 mA p-p with good accuracy ($< 0.5\%$) over a wide frequency range (> 500 kHz). Using custom integrated circuit techniques allows for system miniaturization and potentially better performance than discrete implementations [21]. In [25] we presented the preliminary design of a high power CMOS current driver employing negative feedback (see Fig. 1). The
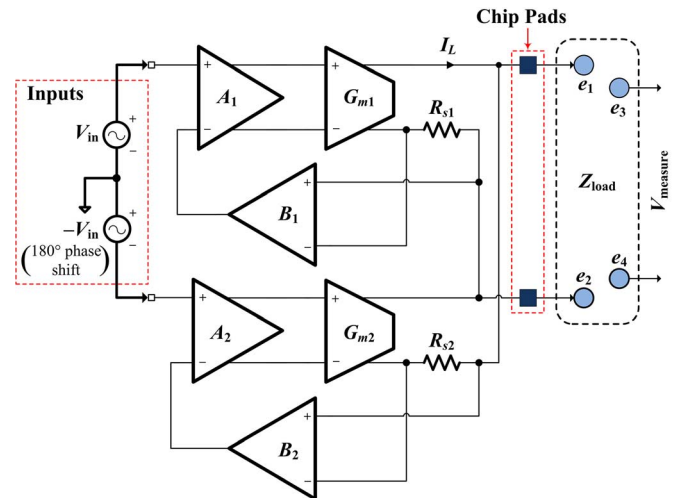

Fig. 1. Proposed current driver topology (electrodes e_1 and e_2 are connected to the output chip pads of the current driver while electrodes e_3 and e_4 connect to a differential amplifier for voltage measurement which is not part of the chip).

negative feedback allows the transconductance of the current driver to be accurately set through the value of a sense resistor, and also regulates the current through the load thus enhancing the overall output impedance. This paper is an expansion of [25] and presents the complete design and test results of the fabricated current driver chip implemented in a 0.6-μm high-voltage (HV) CMOS process technology.

This paper is organized as follows. Section II outlines the architecture and operation of the current driver. Section III describes the circuit design of the system blocks. Section IV examines the frequency response and compensation using a small-signal equivalent model of the current driver circuit. Section V presents measured results from the fabricated chip samples. The concluding remarks of Section VI complete the paper.

II. CURRENT DRIVER ARCHITECTURE

Fig. 1 shows the system block diagram of the current driver topology in which two identical differential feedback current drivers operate in balanced mode to minimize common mode voltage errors across the load (Z_{load}). Each current driver consists of a preamplifier stage (A_1, A_2) followed by a transconductance stage (G_{m1}, G_{m2}). The current through the load is sensed via two integrated resistors (R_{s1}, R_{s2}) and each resulting voltage is fed back to the negative input terminal of the respective preamplifier thus establishing a negative feedback path. Two voltage buffers (B_1, B_2) present in the feedback loop measure the voltages across the sense resistors and also isolate the load from the input signal. The output current is generated via a differential input voltage through which both current drivers receive 180° phase shifted signals (V_{in}, $-V_{\text{in}}$) thus each one is either sourcing or sinking current relative to the other. Assuming a resistive load (R_L) the low frequency transconductance of a single current driver is given by

$$G_{\text{driver}} = \frac{I_L}{V_{\text{in}}} = \frac{1}{R_s + \left(\frac{r_o + R_s + R_L}{r_o} \right) \frac{1}{AG_m}} \quad (1)$$
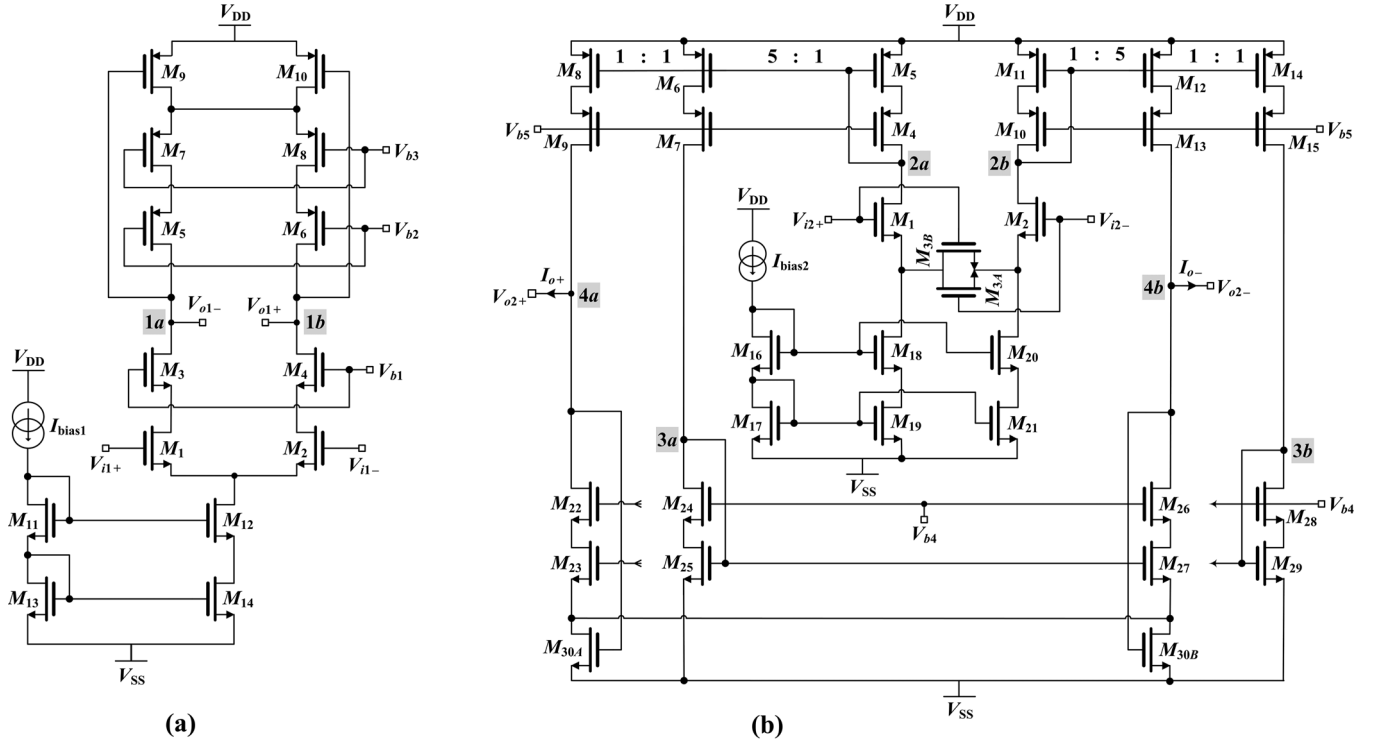
Fig. 2. (a) Transistor level schematic of the preamplifier. (b) Transistor level schematic of the transconductance stage.

where I_L is the load current, A is the voltage gain of the preamplifier, G_m is small-signal gain of the transconductance stage, r_o is the small-signal output resistance of the transconductance stage, and R_s is the sense resistor. If $r_o \gg R_s + R_L$ and $AG_mR_s \gg 1$ then $G_{\text{driver}} \approx 1/R_s$. Hence, if the above conditions are met, G_{driver} can be set according to the value of the sense resistor and thus be independent of the circuit's internal parameters. The total transconductance of the topology in Fig. 1 is twice the transconductance of a single current driver. The single current driver's output resistance is given by

$$R_{\text{out}} = r_o + (AG_mr_o + 1)R_s. \tag{2}$$

The use of negative feedback therefore enhances the circuit's output resistance. The total output resistance is halved because there are two current drivers connected in parallel.

III. CIRCUIT DESIGN

A. Preamplifier

The preamplifier provides an enhancement to G_{driver}. Fig. 2(a) shows the schematic diagram of the preamplifier in which a fully differential cascode topology is used. A cascode current mirror formed by transistors $M_{11} - M_{14}$ provides the input bias tail current to the input differential pair formed by M_1 and M_2 (both 188 μm/2 μm). Transistors $M_3 - M_8$ provide active loading to the input differential pair thus enhancing the circuit's output resistance and differential gain. Bias voltages V_{b1-3} are applied to the cascode pairs to ensure they are operating in the saturation region. All transistors are operating in the saturation region except for M_9 and M_{10} (both 188 μm/2 μm)

which operate in the triode region. Their purpose is to provide a CMFB path to stabilize the dc voltage level at the output [26]. Any drifting of the output dc level is compensated by a change in the voltage across these two triode transistors which effectively act as resistors. The value of the resistance is a function of the transistor's geometry and gate-source voltage. A small change in the output dc voltage level is sensed at the gate of M_9 and M_{10} whose resistance value changes, thus changing the voltage drop across them as the quiescent current flowing is constant. This change in the voltage drop across them is in a direction so as to oppose the change in the output dc voltage level thus establishing a negative feedback loop. However, the proposed CMFB approach has a certain limitation in which the loop gain is small due to the fact that transistors M_9 and M_{10} operate in the triode region and hence, their small-signal transconductance is low. Differential signals do not affect the operation of this loop due to the common mode summation connection between them (drain of transistors M_9 and M_{10}). Transistor dimensions were calculated for minimum overdrive voltage required by the devices for a quiescent current of 500 μA. The preamplifier's nominal open loop differential gain and -3 dB bandwidth are 816 V/V and 2.76 MHz, respectively.

B. Transconductance Stage

Fig. 2(b) shows the schematic diagram of the transconductance stage. The architecture is based on a pseudo-differential balanced scheme. Transistors M_1 and M_2 (both 50 μm/2 μm) biased by current sources M_{19} and M_{21} form the input differential pair whose linearity characteristic is enhanced by the degeneration pair formed by M_{3A} and M_{3B} (both 30 μm/2 μm). High swing cascode current mirrors formed by transistors $M_4 -$
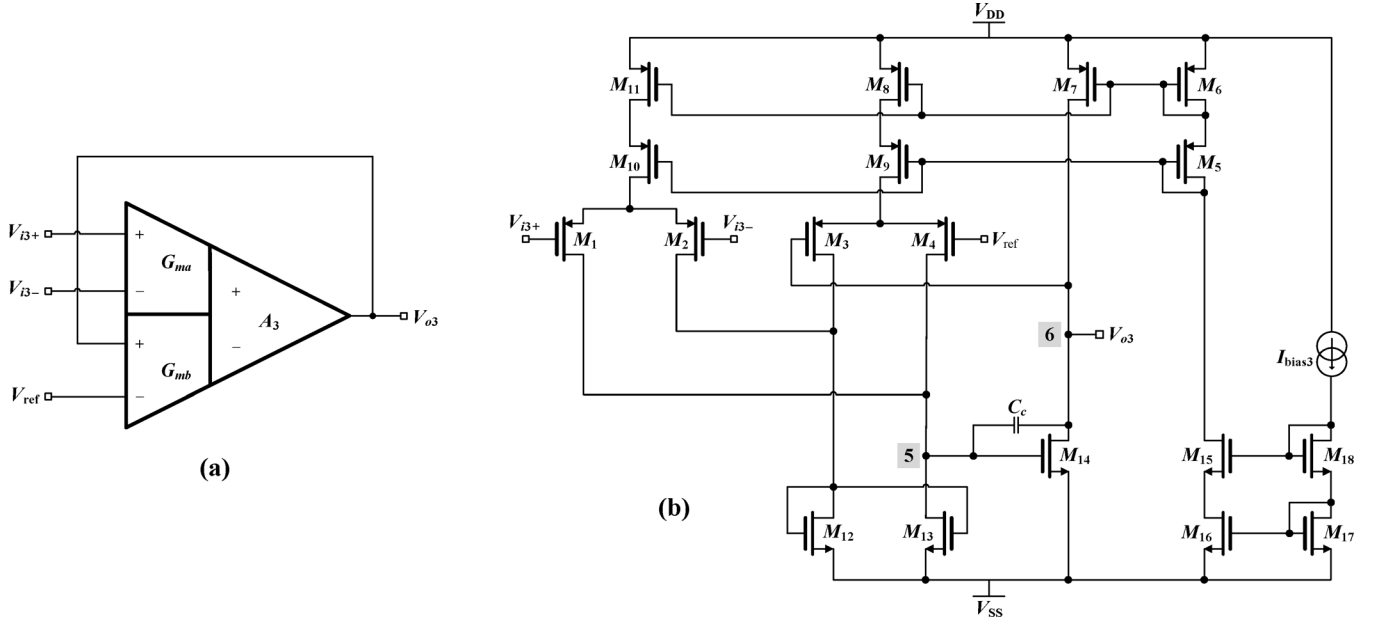
Fig. 3. (a) Unity gain voltage buffer using a differential difference amplifier. (b) Transistor level schematic of the voltage buffer.

$M_8, M_{10} - M_{15}$ and $M_{22} - M_{29}$ provide an increased output resistance and a reduced overdrive voltage compared to their regular cascode counterpart. Transistors M_{30A} and M_{30B} (both 163 μm/2 μm) operate in the triode region and serve the same purpose as transistors M_9 and M_{10} described in the pre-amplifier circuit. The current (single-ended) at the output node is the difference between the current supplied by the PMOS and NMOS current sources. It can be approximated by $I_o \approx BG_{mi}(V_{i2+} - V_{i2-})$ where B (= 5 here) is the current mirror gain factor between M_5 and M_6, M_8 (or M_{11} and M_{12}, M_{14}) as shown in Fig. 2(b), and G_{mi} is transconductance of the source degenerated input stage $(M_1, M_2, M_{3A}, M_{3B})$. The dc bias current (I_{bias2}) is 500 μA and the circuit achieves a maximum output current of 5 mA p-p.

The output voltage compliance of the transconductance circuit in Fig. 2(b) determines the maximum load that the current driver can handle with the maximum output current amplitude of 2.5 mA. However, the allowable injected current amplitude must comply with international safety standards [27]. For frequencies less than 1 kHz where the load magnitude is of the order of 10 kΩ, the maximum allowable current is around 100 μA, which translates to an output voltage compliance of about 2 V. Current amplitudes of 2.5 mA are allowed at frequencies above 25 kHz where the load magnitude is reduced to approximately 1 kΩ, therefore requiring an output voltage compliance of 5 V. The current driver's output voltage compliance (V_{out}) is determined by the effective compliance of the transconductance stage [Fig. 2(b)]. It is given by

$$V_{SS} + V_{M_{30B}} + V_{ovM_{26}} + V_{ovM_{26}} < V_{out} < V_{DD} + V_{ovM_{12}} + V_{ovM_{13}} \quad (3)$$

where V_{SS} and V_{DD} are respectively the positive and negative supply voltages, V_{ovMi} is the overdrive voltage of transistor M_i, and $V_{M_{30B}}$ is the voltage across M_{30B}.

Transistor dimensions were adjusted in order to maximize output voltage compliance. The output voltage compliance is approximately 15 V (some nonlinearities exist near the limits as transistors enter the triode region). This voltage compliance can accommodate a wide range of load impedances, hence making the current driver suitable for a variety of EIT applications. The transconductance stage was designed for a nominal gain of 5.6 mA/V and a -3 dB bandwidth at approximately 13 MHz when the outputs are short-circuited.

C. Voltage Buffer

The purpose of the voltage buffer is to monitor the injected current to the electrode-tissue load by measuring the floating voltage across the sense resistor (R_s). The measured voltage is fed back to the negative input terminal of the preamplifier thus forming a negative feedback loop. As shown in Fig. 1 the voltage buffer is a differential to single ended architecture and the most common topologies are IAs [28], [29]. However, the gain of an IA is typically the ratio of two resistors which have to be tightly matched (for unity gain). To avoid the use of tightly matched resistors the design used a differential difference amplifier (DDA) [30] configured as a differential to single ended unity gain voltage buffer [see Fig. 3(a)]. The DDA features two transconductance elements (G_{ma}, G_{mb}) followed by an amplification stage (A_3). Input to the structure is via the input terminals of the top transconductor. The output terminal is fed back to the positive terminal of the bottom transconductor while the negative terminal is held at a constant reference level (V_{ref}) which is set to 0 V. The negative feedback configuration follows the voltage difference between terminals V_{i3+} and V_{i3-}, which are connected across the sense resistor terminals as shown in Fig. 1. The schematic diagram of the voltage buffer is shown in Fig. 3(b). Transistors $M_1 - M_4$ (all 30 μm/5 μm) form the two input transconductors biased by current sources M_8 and M_{11}. A second amplification stage is formed by transistors M_7 and
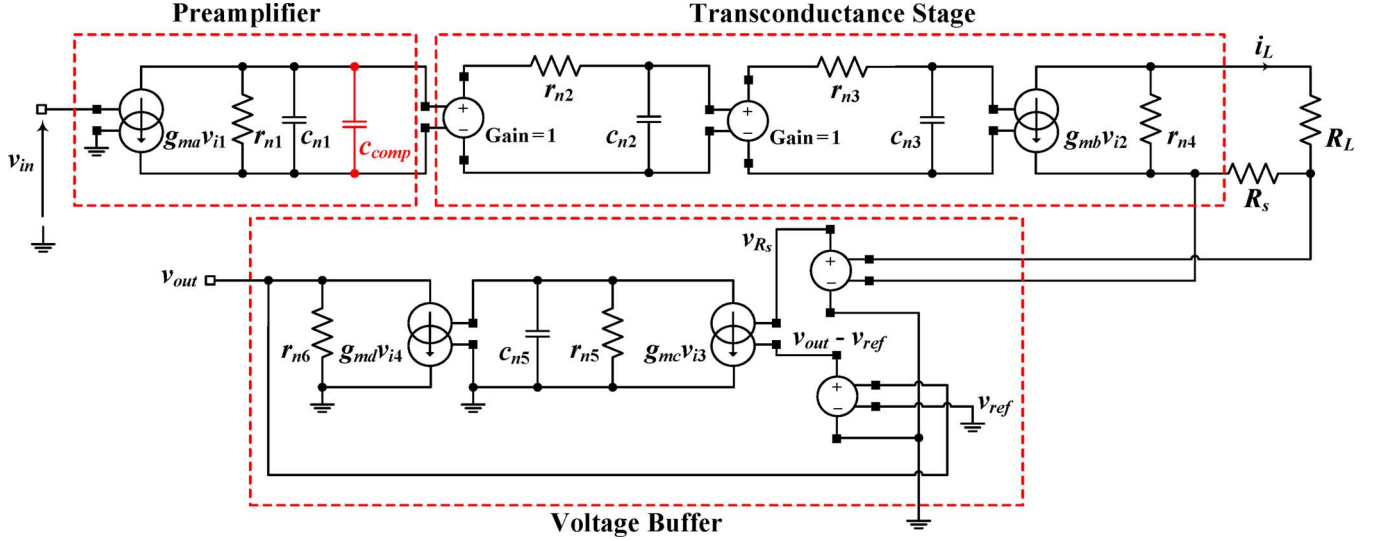
Fig. 4. Small-signal model for calculation of the loop gain.

M_{14}. NMOS current mirror pair M_{12} and M_{13} performs the differential to single ended operation required for the subtraction of the four inputs. The output node is fed back to the gate of transistor M_3 for unity gain and a reference voltage set at 0 V is applied to the gate of M_4. A 1 pF compensation capacitor (C_c) is added for improved phase margin.

The voltage buffer's small-signal voltage gain is given by

$$A_v = \frac{1}{1 + \frac{(g_{o1}+g_{o4}+g_{o13})g_{m13}(g_{o14}+g_{o7})}{g_{m1}g_{m13}g_{m14}}} \quad (4)$$

where g_{mi} and g_{oi} are respectively the small-signal transconductance and output conductance of transistor M_i. The circuit achieves a gain of 0.9958 V/V at dc and is reduced to 0.9946 V/V at 1 MHz.

IV. FREQUENCY COMPENSATION

In order to ensure stability in the negative feedback loop the loop phase response must not exceed the 180° point. The closed-loop transfer function of a negative feedback system is given by

$$T(s) = \frac{A(s)}{1 + A(s)\beta} \quad (5)$$

where the term $A(s)\beta$ is the feedback loop gain. When the phase of the feedback loop becomes $-180°$ at the unity gain frequency of the system, then $A(s)\beta = -1$, and the denominator in (5) becomes zero causing the closed loop transfer function to become infinity. Thus, the system becomes unstable and the output oscillates with increasing amplitude. In order to examine the feedback loop response of our system, a simplified small-signal equivalent circuit of a single current driver was constructed and simulated to verify its performance relative to the transistor-level design. The simplified small-signal equivalent circuit is shown in Fig. 4 with the feedback loop open.[1]

[1]The feedback loop was broken and the negative input of the preamplifier was set to a dc level that matches the output dc level of the voltage buffer which was almost 0 V.

Only capacitances associated with dominant poles are shown as the rest take place at much higher frequencies and do not affect the frequency performance of the system. In the preamplifier [Fig. 2(a)] the dominant poles occur at nodes $1a$ and $1b$, in the transconductance stage [Fig. 2(b)] at nodes $2a, 2b, 3a$ and $3b$, and in the voltage buffer [Fig. 3(b)] at node 5, the latter forming pole p_5. Nodes $1a$ and $1b$ carry signals with the same amplitude but opposite phase. Therefore, nodes $1a$ and $1b$ form one single pole p_1. The same applies to node pairs $(2a, 2b)$ and $(3a, 3b)$ in the transconductance stage, forming poles p_2 and p_3, respectively. In the small-signal model r_{ni} and c_{ni} represent the resistance and capacitance at node n_i, respectively. The terms g_{ma} and g_{mb} denote the small-signal transconductance of the preamplifier and the transconductance stage, respectively. The terms g_{mc} and g_{md} denote the small-signal transconductance of the voltage buffer's input stage and output stage, respectively. The values of the small-signal parameters were obtained using the extracted values from the transistor level circuit in Cadence. The resistors R_L and R_s were set to 1 kΩ and 500 Ω, respectively.

The system's loop gain transfer function is given by

$$\frac{v_{out}}{v_{in}} = \frac{g_{ma}g_{mb}g_{mc}g_{md}r_{n1}r_{n5}r_{n6}R_s}{p_1p_2p_3(p_5 + g_{mc}g_{md}r_{n5}r_{n6})}. \quad (6)$$

The position of the four poles p_1, p_2, p_3, and p_5 of the uncompensated loop gain were evaluated at $f_{p1} = 916$ kHz, $f_{p2} = 13.26$ MHz, $f_{p3} = 205.8$ MHz, and $f_{p5} = 13.55$ MHz, and the unity gain frequency point at approximately 53 MHz. Pole p_3 could be neglected as it takes place at a very high frequency, yielding a three-pole system. Poles p_2 and p_5 take place at really close frequency points. This results in an excess of 180° phase shift as p_2 and p_5 take place before the unity gain frequency point thus causing system instability. Placing a capacitor (c_{comp}) between the preamplifier and the transconductance stage provides dominant pole compensation. A 60 pF on-chip compensation capacitor, added at the output terminals of the preamplifier, created a dominant pole at approximately 7 kHz, yielding sufficient phase-margin for stability in practice.

TABLE I
CHIP PERFORMANCE PARAMETERS AND COMPARISON WITH PREVIOUS WORK

	[12]	[32]	[15]	[19]	[21]	This work
Architecture	Modified Howland	Modified Howland*	Current Conveyor	Differential Current Generator	Differential OTA	Negative Feedback
Maximum Output Current	$1\,\mathrm{mA_{p\text{-}p}}$	$5\,\mathrm{mA_{p\text{-}p}}$	$>1\,\mathrm{mA_{p\text{-}p}}$	$350\,\mathrm{\mu A_{p\text{-}p}}$	$500\,\mathrm{\mu A_{p\text{-}p}}$	$5\,\mathrm{mA_{p\text{-}p}}$
Bandwidth	$1\,\mathrm{kHz} - 1\,\mathrm{MHz}$	$1\,\mathrm{kHz} - 1\,\mathrm{MHz}$	$10\,\mathrm{kHz} - 250\,\mathrm{kHz}$	$90\,\mathrm{kHz}$	$10\,\mathrm{kHz} - 1\,\mathrm{MHz}$	$>500\,\mathrm{kHz}$
Output Impedance	$670\,\mathrm{k\Omega}$ @ $100\,\mathrm{kHz}$ $330\,\mathrm{k\Omega}$ @ $300\,\mathrm{kHz}$	$>64\,\mathrm{M\Omega}$ @ dc $<500\,\mathrm{k\Omega}$ @ $50\,\mathrm{kHz}$	$149\,\mathrm{k\Omega}$ @ $100\,\mathrm{kHz}$ $<30\,\mathrm{k\Omega}$ @ $500\,\mathrm{kHz}$	$>100\,\mathrm{k\Omega}$ @ $90\,\mathrm{kHz}$	$>1\,\mathrm{M\Omega}$ @ $100\,\mathrm{kHz}$ $>500\,\mathrm{k\Omega}$ @ $500\,\mathrm{kHz}$	$665\,\mathrm{k\Omega}$ @ $100\,\mathrm{kHz}$ $372\,\mathrm{k\Omega}$ @ $500\,\mathrm{kHz}$
THD	----------	----------	0.45% @ $1\,\mathrm{mA_{p\text{-}p}}$	0.81% @ $250\,\mathrm{\mu A_{p\text{-}p}}$	0.79% @ $500\,\mathrm{\mu A_{p\text{-}p}}$	0.69% @ $5\,\mathrm{mA_{p\text{-}p}}$ 0.53% @ $2\,\mathrm{mA_{p\text{-}p}}$
Supply Voltage	----------	----------	$30\,\mathrm{V}$	$1.2\,\mathrm{V} \sim 1.5\,\mathrm{V}$	$5\,\mathrm{V}$	$18\,\mathrm{V}$
Technology	Discrete	Discrete	Discrete	$0.18\text{-}\mu\mathrm{m}$ CMOS	$0.35\text{-}\mu\mathrm{m}$ CMOS	$0.6\text{-}\mu\mathrm{m}$ CMOS HV

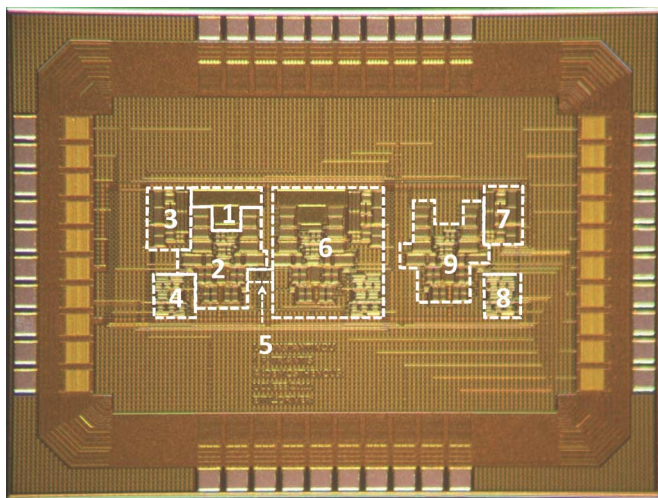*With resistor calibration and negative capacitance calibration

Fig. 5. Chip microphotograph with main circuit blocks numbered. (1) Compensation capacitor. (2) OTA. (3) Preamplifier. (4) Voltage buffer. (5) Sense resistors. (6) Second current driver. (7) Preamplifier test structure. (8) Voltage buffer test structures. (9) Transconductance stage test structure.

Fig. 6. Transconductance of current driver versus input voltage at 100 kHz for eleven chips for a load of 1 kΩ//4.3 pF.

V. MEASURED RESULTS

The current driver was designed and fabricated in a 0.6-μm CMOS HV process technology [31]. The design and layout were performed with Cadence software. Each of the two on-chip sense resistors were chosen to be 500 Ω, yielding a nominal total transconductance of 4 mA/V. The fabricated chip microphotograph is shown in Fig. 5 with the main components numbered. The size of the core area is 0.64 mm^2. The total chip area including pads and test structures is 6.18 mm^2. The tests performed aimed to study the circuit's transconductance over the required input voltage range as well as the accuracy of the output current over frequency. Other parameters such as output impedance and total harmonic distortion (THD) were evaluated and are reported in Table I. All of the eleven chips operated satisfactorily. The chip was mounted on a purpose-built printed circuit board providing the necessary bias currents as well as input/output signals to the circuit. The circuit was operated from a ±9 V power supply.
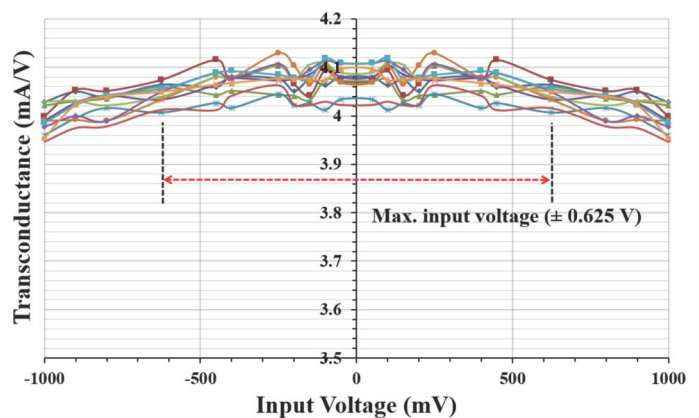
The input voltage signals to the current driver chip were controlled via a TTi TGA12101 signal generator, able to operate up to 40 MHz. Fig. 6 shows the measured transconductance as a function of the input voltage at a frequency of 100 kHz. The signal generator was used to generate input voltage signals of amplitude up to 1 V. An on-board AD8253 IA with variable gain settings from Analog Devices, able to operate up to 10 MHz with unity gain setting, was used to measure the differential voltage developed across the load impedance. The output voltage was monitored using an Agilent Infinii Vision oscilloscope. The transconductance was then evaluated with a load of 1 kΩ//4.3 pF at a frequency of 100 kHz. The maximum input voltage corresponding to the maximum output current amplitude of 2.5 mA is ±0.625 V. The measured results confirm an average transconductance value of 4.07 mA/V with a standard deviation of 0.012 mA/V and a maximum spread of 1% for all eleven chips, within the maximum input voltage range. The average value of the transconductance deviates by a maximum of 1.7% of the nominal value (4 mA/V) which can be attributed to fabrication errors of the value of the sense resistors.

Fig. 7 shows the measured output current at amplitudes of 0.5 mA, 1 mA and 2.5 mA for the eleven chips over the frequency range of 10 kHz to 5 MHz with a load of 1 kΩ//4.3 pF. In the frequency range 10 kHz to 500 kHz the accuracy of the
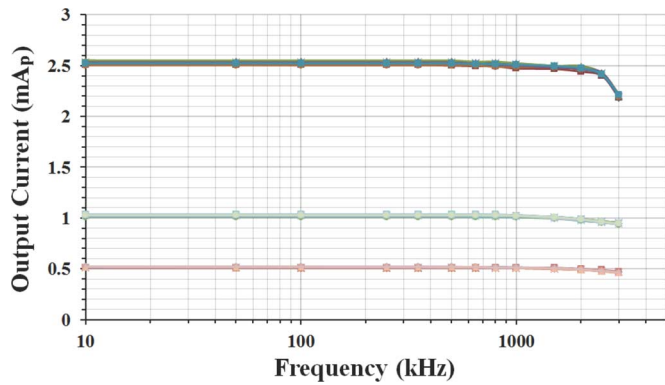
Fig. 7. Output current amplitude versus frequency for eleven chips at amplitudes of 0.5 mA, 1 mA, and 2.5 mA.

Fig. 8. Current driver output voltage compliance.

output current is of the order of 0.15% for 0.5 mA, 0.22% for 1 mA and 0.41% for 2.5 mA. Between 10 kHz and 1 MHz the accuracy of the output current is of the order of 0.15% for 0.5 mA, 0.23% for 1 mA and 0.47% for 2.5 mA.

The THD of the current driver was evaluated using an Agilent E4411B spectrum analyzer at 500 kHz. THD results were taken for three different input voltage amplitude levels, corresponding to 0.5 mA, 1 mA and 2.5 mA output current amplitudes, and the power from ten harmonic frequencies was measured each time. The measured THD for 0.5 mA was 0.52%, 0.53% for 1 mA and 0.69% for 2.5 mA. The IA's THD at 500 kHz had a negligible effect on the measurements.

The output impedance performance of the current driver was measured for frequencies between 100 kHz and 1 MHz as lower frequency measurements were not possible due to equipment limitations. The output impedance was measured by varying the load magnitude between two values of 100 Ω and 5.1 kΩ and recording the change in the measured output voltage with the output current set to 200 μA. The output impedance magnitude was calculated by

$$Z_{\text{out}} = \left| \frac{(V_2 - V_1)R_{L1}R_{L2}}{(V_2 R_{L1}) - (V_1 R_{L2})} \right| \tag{7}$$

where V_1 and V_2 are the two individual voltage readings and R_{L1} and R_{L2} are the two load values.

The associated parasitic capacitance was 4.7 pF, measured with a Wayne Kerr 6500B impedance analyzer, which was incorporated in order to evaluate the magnitude of the load impedance at every frequency point. The associated parasitic capacitance was measured between the two chip output pads shown in Fig. 1 where the two load values were connected across. A toggle switch was used to switch between the two values and its associated parasitic capacitance was also measured and incorporated into the total value. The measured output impedance was approximately 665 kΩ at 100 kHz reducing to 372 kΩ at 500 kHz and 64 kΩ at 1 MHz. It should be noted, however, that the above method to determine the output impedance is very sensitive to small variations in the measured signals. The accuracy of the output impedance measurement is $\pm$15% at 100 kHz, $\pm$10% at 500 kHz and $\pm$2% at 1 MHz.
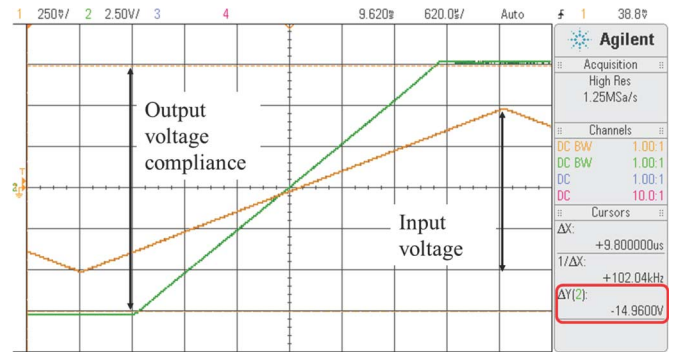
The input/output phase delay was evaluated at a frequency range between 10 kHz and 1 MHz. Input/output phase delay characteristic of the chip presents an important feature especially for bioimpedance measurements as determination of the load impedance phase is crucial. Hence, in cases where the phase shift caused by the instrumentation is not taken into account it can lead to erroneous load impedance estimations. The input/output phase response was measured to be 0.37° at 10 kHz, 0.7° at 100 kHz, 8° at 500 kHz and 12° at 1 MHz. The phase shift introduced by the IA was also characterized and subtracted from the total recorded value.

Fig. 8 shows the output voltage compliance of the current driver when driving a load of 5.1 kΩ and varying the input voltage amplitude. The allowable voltage compliance was measured to be approximately 15 V. Table I summarizes the main performance characteristics along with a comparison with previous work. The presented current driver provides higher output current and compliance range and lower THD compared with other integrated designs. Its output impedance at high frequencies (500 kHz) is superior to all except [21] which has added active load compensation and is restricted to fabrication in certain technologies.

VI. CONCLUSION

A high power integrated current driver implemented in a 0.6-μ m standard HV CMOS technology has been presented. The circuit features a pair of balanced current drivers in a negative feedback configuration for monitoring and regulating the output current. The negative feedback offers the possibility of accurately setting the transconductance of the current driver with reference to the sense resistor independent of the circuit's other internal parameters. The constant transconductance feature was tested and verified with a mean value of 4.07 mA/V and a standard deviation of 0.012 mA/V for an input voltage of $\pm$0.625 V, which translates to the maximum allowable output current. The maximum spread between eleven chips is 1%. The result confirms not only a constant value within the required input range but also a reasonably good matching between different chips in a single fabrication run which is adequate for our application. In the case of active electrode EIT imaging, an array of electrode pairs are driven by individual chips and a high degree of matching between them is essential. For superior matching laser trimming or some calibration might be

necessary. The current driver can deliver an output current of 5 mA p-p with an accuracy of 0.41% in the frequency range between 10 kHz and 500 kHz and a maximum THD of 0.69%. The allowable voltage compliance makes the circuit suitable for driving a wide range of load impedances for high output current applications. The circuit has an output impedance of the order of 372 kΩ at 500 kHz. The fabricated chip occupies a core area of 0.64 mm^2. The chip is primarily intended for a parallel current drive EIT system implemented as a wearable device using active electrodes for neonatal lung function monitoring in intensive care units. It is also suitable for other EIT and bioimpedance applications [1] requiring wideband, accurate current drivers.

REFERENCES

[1] R. Bayford and A. Tizzard, "Bioimpedance imaging: An overview of potential clinical applications," *Analyst*, vol. 137, pp. 4635–4643, 2012.

[2] D. Murphy, P. Burton, R. Coombs, L. Tarassenko, and P. Rolfe, "Impedance imaging in the newborn," *Clin. Phys. Physiol. Meas.*, vol. 8, pp. 131–140, 1987.

[3] A. Taktak, A. Spencer, P. Record, R. Gadd, and P. Rolfe, "Feasibility of neonatal lung imaging using electrical impedance tomography," *Early Human Develop.*, vol. 44, pp. 131–138, 1996.

[4] B. H. Brown, R. A. Primhak, R. H. Smallwood, P. Milnes, A. J. Narracott, and M. J. Jackson, "Neonatal lungs: Can absolute lung resistivity be determined non-invasively," *Med. Biol. Eng. Comput.*, vol. 40, pp. 388–394, 2002.

[5] R. J. Halter, A. Hartov, and K. D. Paulsen, "A broadband high-frequency electrical impedance tomography system for breast imaging," *IEEE Trans. Biomed. Eng.*, vol. 55, pp. 650–659, 2008.

[6] J. C. Baeg, H. Wi, T. I. Oh, A. L. McEwan, and E. J. Woo, "An amplitude-to-time conversion technique for multichannel data acquisition and bioimpedance imaging," *IEEE Trans. Biomed Circuits Syst.*, vol. 7, no. 3, pp. 349–354, 2013.

[7] R. Bayford, P. Kantartzis, A. Tizzard, R. Yerworth, P. Liatsis, and A. Demosthenous, "Development of a neonate lung reconstruction algorithm using a wavelet AMG and estimated boundary form," *Physiol. Meas.*, vol. 29, pp. 125–138, 2008.

[8] M. Rahal, J. M. Khor, A. Demosthenous, A. Tizzard, and R. Bayford, "A comparison study of electrodes for neonate electrical impedance tomography," *Physiol. Meas.*, vol. 30, pp. S73–S84, 2009.

[9] J. Rosell, J. Colominas, P. Riu, R. Pallas-Areny, and J. G. Webster, "Skin impedance from 1 Hz to 1 MHz," *IEEE Trans. Biomed. Eng.*, vol. 35, pp. 649–651, 1988.

[10] S. Franco, *Design With Operational Amplifiers and Analog Integrated Circuits*. New York, NY, USA: McGraw-Hill Higher Education, 2003.

[11] A. S. Tucker, R. M. Fox, and R. J. Sadleir, "Biocompatible, high precision, wideband, improved Howland current source with lead-lag compensation," *IEEE Trans. Biomed. Circuits Syst.*, vol. 7, no. 1, pp. 63–70, 2013.

[12] P. Bertemes-Filho, B. H. Brown, and A. J. Wilson, "A comparison of modified Howland circuits as current generators with current mirror type circuits," *Physiol. Meas.*, vol. 21, pp. 1–6, 2000.

[13] C. W. Denyer, F. J. Lidgey, Q. S. Zhu, and C. N. McLeod, "High output impedance voltage controlled current source for bio-impedance instrumentation," in *Proc. 15th Annu. Int. Conf. IEEE Engineering in Medicine and Biology Soc.*, San Diego, CA, USA, 1993, pp. 1026–1027.

[14] F. Seoane, R. Bragos, and K. Lindecrantz, "Current source for multifrequency broadband electrical bioimpedance spectroscopy systems. A novel approach," in *Proc. 28th Annu. Int. Conf. IEEE Engineering in Medicine and Biology Soc.*, New York, NY, USA, 2006, pp. 5121–5125.

[15] O. Casas, J. Rosell, R. Bragos, A. Lozano, and P. J. Riu, "A parallel broadband real-time system for electrical impedance tomography," *Physiol. Meas.*, vol. 17, pp. 1–6, 1996.

[16] R. D. Cook, G. J. Saulnier, D. G. Gisser, J. C. Goble, J. C. Newell, and D. Isaacson, "ACT3: A high-speed, high-precision electrical impedance tomograph," *IEEE Trans. Biomed. Eng.*, vol. 41, pp. 713–722, 1994.

[17] N. Terzopoulos, K. Hayatleh, B. Hart, F. J. Lidgey, and C. McLeod, "A novel bipolar-drive circuit for medical applications," *Physiol. Meas.*, vol. 26, pp. 21–27, 2005.

[18] J. Frounchi, F. Dehkhoda, and M. H. Zarifi, "A low-distortion wideband integrated current source for tomography applications," *Eur. J. Sci.. Res.*, vol. 27, pp. 56–65, 2009.

[19] L. Yan, J. Bae, S. Lee, T. Roh, K. Song, and H. J. Yoo, "A 3.9 mW 25-electrode reconfigured sensor for wearable cardiac monitoring system," *IEEE J. Solid-State Circuits*, vol. 46, pp. 353–364, 2011.

[20] P. Bertemes-Filho, V. C. Vincence, M. M. Santos, and I. X. Zanatta, "Low power current sources for bioimpedance measurements: A comparison between Howland and OTA-based CMOS circuits," *J. Electr. Bioimp.*, vol. 3, pp. 66–73, 2012.

[21] H. Hong, M. Rahal, A. Demosthenous, and R. Bayford, "Comparison of a new integrated current source with the modified Howland circuit for EIT applications," *Physiol. Meas.*, vol. 30, pp. 999–1007, 2009.

[22] J. H. Li, C. Joppek, and U. Faust, "Fast EIT data acquisition system with active electrodes and its application to cardiac imaging," *Physiol. Meas.*, vol. 17, pp. 25–32, 1996.

[23] P. O. Gaggero, A. Adler, J. Brunner, and P. Seitz, "Electrical impedance tomography system based on active electrodes," *Physiol. Meas.*, vol. 33, pp. 831–847, 2012.

[24] J.-M. Khor, R. H. Bayford, A. Tizzard, and A. Demosthenous, Boundary Shape Estimation of Infant Thorax Using Flexible Sensors to Minimize Lung Artefacts Reconstructed from Electrical Impedance Tomography, U.S. application no. 61/867,904, Aug. 23, 2013.

[25] L. Constantinou, A. Demosthenous, P. Langlois, R. Bayford, and I. Triantis, "An improved CMOS current driver for electrical impedance tomography," in *Proc. 20th Eur. Conf. Circuit Theory and Design*, Linköping, Sweden, 2011, pp. 290–293.

[26] F. Krummenacher and N. Joehl, "A 4-MHz CMOS continuous-time filter with on-chip automatic tunning," *IEEE J. Solid-State Circuits*, vol. 23, pp. 750–758, 1988.

[27] Medical Electrical Equipment—Part 1: General Requirements for Basic Safety and Essential Performance, 3rd ed., IEC60601-1, 2005.

[28] A. Worapishet, A. Demosthenous, and X. Liu, "A CMOS instrumentation amplifier with 90-dB CMRR at 2-MHz using capacitive neutralization: Analysis, design considerations, and implementation," *IEEE Trans. Circuits Syst. I, Reg, Papers*, vol. 58, pp. 699–710, 2011.

[29] Y. Zhao, A. Demosthenous, and R. Bayford, "A CMOS instrumentation amplifier for wideband spectroscopy systems," in *Proc. IEEE Int. Symp. Circuits Systems*, Kos Island, Greece, 2006, pp. 5079–5082.

[30] E. Sackinger and W. Guggenbuhl, "A versatile building block: The CMOS differential difference amplifier," *IEEE J. Solid-State Circuits*, vol. 22, pp. 287–294, 1987.

[31] X-FAB Semiconductor Foundries AG Germany [Online]. Available: http://www.xfab.com

[32] J. W. Lee, T. I. Oh, S. M. Paek, J. S. Lee, and E. J. Woo, "Precision constant current source for electrical impedance tomography," in *Proc. 25th Annu. Int. Conf. IEEE Engineering in Medicine and Biology Soc.*, Cancun, Mexico, 2003, pp. 1066–1069.

Loucas Constantinou (S'10) was born in Limassol, Cyprus, in 1986. He received the M.Eng. degree (with first class honours) in biomedical engineering from Imperial College, London, U.K., in 2010.

He then joined the Analog and Biomedical Electronics Group in the Department of Electronic and Electrical Engineering, University College London (UCL), London, U.K., where he is working toward the Ph.D. degree in the area of bioimpedance spectroscopy. He was awarded a UCL studentship funded by the Engineering and Physical Sciences Research Council (EPSRC). His research interests are in the area of analog integrated circuit design for biomedical applications, wideband ac current drivers, and electrical impedance tomography.

Iasonas F. Triantis (M'02) was born in Geneva, Switzerland, in 1976. He received the M.Eng. degree in electronic engineering from MIST, Manchester, U.K., and the Ph.D. degree in electronic engineering from University College London (UCL), London, U.K., in 2000 and 2005, respectively.

He was a Research Assistant at UCL until 2005, working on implantable neuroprosthetics and neural interfacing. He was a Research Associate with Imperial College London, London, U.K., until 2010, where he continued work on neural recording and stimulation chips, and researched alternative neural interfacing methods that could be used in both the peripheral and the central nervous system. He then returned to UCL as a Senior Research Associate to work on electrical impedance tomography microelectronic systems for neonatal lung monitoring. Since 2012, he has been a Lecturer in the School of Engineering and Mathematical Sciences, City University, London, U.K., specializing in instrumentation and sensors for bio-interfacing research within the Bioengineering Research Group. He has authored eight journal and 27 conference publications, three book chapters, an IEEE newsletter, and holds three patents.

Richard Bayford (M'85) received the M.Sc. degree in industrial systems from Cranfield University, Cranford, Bedforshire, U.K., and the Ph.D. degree from Middlesex University, London, U.K., in 1994.

From 1973 to 1979, he held a post at Marconi Space Defense Systems before moving to academia. He was appointed Professor of bio-modeling and informatics in 2005 in the Department of Natural Sciences, Middlesex University, and also holds an honorary post in the Department of Electrical and Electronic Engineering, University College London. His expertise is in biomedical image/signal processing, electrical impedance tomography (EIT), nanotechnology, deep brain stimulation, bio-modeling, tele-medical systems, sensors, and VLSI design. His current research focus is the development of reconstruction algorithms and hardware for new imaging methods for the detection of cancer biomarkers. Recently, he has adapted this research area to addressing the problem of modeling electrical field distribution in the human head for deep brain stimulation. He has also pioneered the first reconstruction algorithm to image impedance changes inside the human head.

Dr. Bayford has authored over 200 papers in journals and international conference proceedings. He has been a Guest Editor on four special issues and co-organizer of three conferences on biomedical applications of EIT. He is the Editor-in-Chief of *Physiological Measurement*, Institute of Physics, and serves on the editorial board of the *International Journal of Biomedical Imaging*. He is the Chair of the publication committee of the Institute of Physics and Engineering in Medicine (IPEM).

Andreas Demosthenous (S'94–M'99–SM'05) received the B.Eng. degree in electrical and electronic engineering from the University of Leicester, Leicester, U.K., the M.Sc. degree in telecommunications technology from Aston University, Birmingham, U.K., and the Ph.D. degree in electronic and electrical engineering from University College London (UCL), London, U.K., in 1992, 1994, and 1998, respectively.

He was a Postdoctoral Research Fellow with the Department of Electronic and Electrical Engineering, UCL, from 1998 to 2000. He became an academic faculty member in 2000, and is currently a Professor leading the Analog and Biomedical Electronics Research Group. He has numerous collaborations for interdisciplinary research. He has authored or coauthored more than 180 articles in journals and international conference proceedings. His current research interests include analog and mixed-signal integrated circuits for biomedical, sensor, and signal-processing applications.

Dr. Demosthenous is an Associate Editor of the IEEE TRANSACTIONS ON BIOMEDICAL CIRCUITS AND SYSTEMS and the *IEEE Circuits and Systems Newsletter*. He was an Associate Editor of the IEEE TRANSACTIONS ON CIRCUITS AND SYSTEMS I: REGULAR PAPERS from 2008 to 2012. He was recently appointed the Deputy Editor-in-Chief of the IEEE TRANSACTIONS ON CIRCUITS AND SYSTEMS II: EXPRESS BRIEFS and was an Associate Editor of the same journal from 2006 to 2007. He is on the International Advisory Board of *Physiological Measurement*, Institute of Physics. He is a member of the Analog Signal Processing Technical Committee and the Biomedical Circuits and Systems Technical Committee of the IEEE Circuits and Systems Society. He is a member of the Technical Programme Committee of various IEEE conferences including ESSCIRC and VLSI-SoC. He was on the organizing committee of the 2013 IEEE Biomedical Circuits and Systems Conference (BioCAS 2013). He is a Fellow of the Institution of Engineering and Technology and a Chartered Engineer.